Eur. Phys. J. D **7**, 577–586 (1999)

THE EUROPEAN PHYSICAL JOURNAL D

EDP Sciences

Structural characterization of Rh/pumice SMAD catalysts

A. Balerna[1], S. Coluccia[2], G. Deganello[3,4], A. Longo[3,4], A. Martorana[3,4,a], G. Martra[2], C. Meneghini[1], P. Pertici[5], G. Pipitone[3,4], E. Pitzalis[5], A.M. Venezia[3], A. Verrazzani[5], and G. Vitulli[5]

[1] Istituto Nazionale di Fisica Nucleare, Laboratori Nazionali di Frascati, via E. Fermi 40, 00044 Frascati, Italy
[2] Dipartimento di Chimica Inorganica, Fisica e dei Materiali, Università di Torino, via P. Giuria 7, 10125 Torino, Italy
[3] Istituto di Chimica e Tecnologia dei Prodotti Naturali del CNR, via Ugo La Malfa 153, 90146 Palermo, Italy
[4] Dipartimento di Chimica Inorganica, Università di Palermo, viale delle Scienze, 90128 Palermo, Italy
[5] Centro CNR Macromolecole Stereordinate ed Otticamente Attive, Dipartimento di Chimica e Chimica Industriale, Università di Pisa, via Risorgimento 35, 56100 Pisa, Italy

Received 2 February 1999

Abstract. The structure of Rh/pumice catalysts prepared by the SMAD (Solvated Metal Atoms Dispersion) technique at different metal loadings has been investigated by EXAFS (Extended X-ray Absorption Fine Structure Spectroscopy), XPS (X-ray Photoelectron Spectroscopy), SAXS (Small-Angle X-ray Scattering), WAXS (Wide-Angle X-ray Scattering) and TEM (Transmission Electron Microscopy). According to EXAFS and XPS, a fraction of the Rh atoms is oxidised, but a noticeable part is also present as Rh^0. The Rh oxidation is attributed to the interaction of the Rh atoms with the hydroxyls of the support; after the formation of the oxide, the nucleation of metallic rhodium becomes possible. The WAXS data do not show evidence of rhodium *fcc* crystallites; the metal-bearing particles are probably amorphous and/or very small, as results from the SAXS and TEM data analysis. The disagreement between the latter two techniques, resulting in a small-angle determination of the average size of the particles that is about half that of TEM in the catalyst with the higher Rh loading, is acknowledged and discussed. Preliminary catalytic tests are described, demonstrating the suitability of using a low surface area support for the preparation of SMAD catalysts.

PACS. 61.10.Eq X-ray scattering (including small-angle scattering) – 61.10.Ht X-ray absorption spectroscopy: EXAFS, NEXAFS, XANES, etc. – 61.16.Bg Transmission, reflection and scanning electron microscopy (including EBIC)

1 Introduction

Pumice is an amorphous foam produced during volcanic eruptions. It is constituted mostly of silica and alumina in relative amounts varying according to the geological area of origin, and also includes other chemical species, such as different oxides and water [1]. The pumice powder has been recently exploited as a support for metal catalysts [2,3]: to this respect, its striking characteristic is the very low specific surface (about 1 m^2/g, by small-angle X-ray scattering [1]), completely antithetical to what is usually sought in a catalyst carrier. Despite the small surface area, the mono- and bimetallic catalysts supported on the pumice of Lipari (Italy) [3,4] display interesting properties, comparable or even better than the performances of catalysts supported on conventional carriers. In fact, the small surface area allows easy transport of reactants and products, while the high dispersion of the metal phase can be achieved by suitable synthesis techniques. In particular, pumice-supported Pd catalysts prepared by organometallic precursors showed high activity and selectivity in the hydrogenation of highly unsaturated hydrocarbons [3,5]; this property has been demonstrated to be due to the effect of sodium-bearing chemical species present in the support framework [6,7].

Among the noble metal-based catalysts, rhodium systems are the most widely employed, especially in hydrogenation [8], hydroformylation [9] and hydrosilylation [10] reactions. Rhodium catalysts supported on inorganic oxides can be prepared by different techniques such as impregnation with rhodium trichloride [11,12] or anchoring of Rh dimer complexes to the support oxygens [13]. In order to obtain a deeper insight into pumice supported transition metal catalysts, and to exploit a further route for the achievement of high metal dispersion on low surface area carriers, we have prepared rhodium-pumice systems using arene solvated Rh atoms as a source of Rh particles. Solvated metal atoms, obtained by reaction of vaporised metal with weakly stabilizing organic solvents [14], are of great interest as homogeneous catalysts [15,16]

[a] e-mail: nino@ictpn.pa.cnr.it

and as suitable precursors for the deposition of active metal clusters onto a wide range of organic and inorganic supports [14–20].

As already pointed out in the early studies on these materials, the organometallic compounds produced by SMAD (Solvated Metal Atoms Dispersion) are highly oxygen-sensitive, may be even pyrophoric or form oxidised species through interaction with the surface hydroxyls [21] of commonly employed supports such as silica and alumina. In Co–Mn/SiO_2 bimetallic SMAD catalysts [21], for instance, Mn, which is catalytically inactive, has been used for protecting Co from the direct contact with the support oxygen moieties.

The structural studies on heterogeneous catalysts [22], and on SMAD systems in particular, involve different techniques, ranging from spectroscopies to electron microscopy and X-ray scattering. WAXS on SMAD catalysts usually give only the information that the supported metal particles are so small and/or so disordered that no useful diffraction signal can be detected; positive structural data concerning the immediate surrounding of the catalyst atoms can be provided by EXAFS, while XPS allows further evidences concerning the chemistry of the investigated compounds. Size and shape of the particles can be determined by TEM; to the best of our knowledge, no SAXS studies have been carried out on SMAD catalysts. The above quoted techniques (EXAFS, XPS, WAXS, SAXS, TEM) are exploited in the present study and the results contribute to give an overall picture of the structure of the investigated catalysts and of the interaction of the metal phase with the support.

Finally, preliminary catalytic tests on the hydrosilylation of benzonitrile, involving in particular a comparison with a rhodium/γ-Al_2O_3 commercial catalyst and a rhodium/γ-Al_2O_3 SMAD system, are also described, to give a first insight about the suitability of the investigated Rh/pumice systems.

2 Experimental

2.1 Sample preparation

All the operations concerning the preparation and the manipulation of the catalysts have been performed under argon atmosphere.

The pumice powder, of grain size less than 75 μm, to be used as a catalyst carrier has been boiled in dilute HNO_3 to eliminate the surface impurities and then dried in an oven and stored in argon. Its specific surface area, as determined by SAXS [1], is about 1 m^2/g, and the exposed OH content has been determined by LiH titration as 5 ml H_2/g. Commercial γ-Al_2O_3 (AKZO 000-3P product, specific surface area of 180 m^2/g), dried in an oven before use, was exploited for the synthesis of a 0.8 wt% Rh SMAD catalyst, to be used for comparison with the pumice supported ones.

The rhodium/pumice SMAD samples have been prepared by impregnation of the support with mesitylene solvated Rh atoms obtained by cocondensation of Rh vapour and mesitylene at 77 K. The stages of the preparation follow the route previously outlined [17,18]. By varying the quantity of solvated Rh with respect to the support, four catalysts, indicated as A, B, C, D at the respective metal loading of 0.80, 0.46, 0.43 and 0.08 wt% (as determined by an ICP-MS HP4500 mass spectrometer) have been obtained and stored under argon.

The rhodium/γ-Al_2O_3 sample (0.8 wt%) has been prepared following the same experimental procedure. The commercial rhodium/γ-Al_2O_3 sample (3 wt%) is supplied by Engelhard. Benzonitrile (Aldrich product) was distilled from sodium metal. Trimethylsilane was prepared by reaction of trimethylchlorosilane and lithium aluminun hydride according to the literature [23].

2.2 X-ray absorption

The pumice supported samples were prepared for the EXAFS experiments by suspending the fine powder of the samples in ethanol 99.99% and depositing it on millipore membranes under N_2 atmosphere to avoid any oxidation coming from air contamination. The samples have been enveloped with a kapton film. The EXAFS measurements at the Rh K-edge (25.315 keV) were performed at the European Synchrotron Radiation Facility (ESRF) on the Italian beamline GILDA. The monochromator operated with Si(311) crystals in dynamical sagittal focusing mode [24,25]. The energy resolution and flux were approximately 2 eV and 10^{10} photons/s on the sample. Harmonic rejection was performed by using Pt mirrors as a low pass filter (energy cut-off at $\sim$ 27 keV). Two reference samples (α-Rh_2O_3 powder and Rh foil) and the above described four SMAD Rh/pumice catalyst samples were examined. All EXAFS measurements were performed at room temperature. The reference samples were measured in transmission geometry using two Ar filled ionisation chambers to detect the incident (I_0) and transmitted (I_t) beam. The experimental absorption signal is defined as $\mu(E) = \ln(I_0/I_t)$. The EXAFS measurements on SMAD Rh/pumice catalyst were performed in the fluorescence geometry, which is the most suitable in the case of low concentration and/or highly dispersed samples, under 10^{-4} torr vacuum. The fluorescence signal (I_f) was detected using a large area Si PIN diode and the absorption signal was calculated as: $\mu(E) = I_f/I_0$.

2.3 X-ray photoelectron spectroscopy

The X-ray photoelectron analyses were performed with a VG Escalab 200 (Vacuum generator Ltd., UK) equipped with an aluminum anode as a unmonochromatised X-ray source (1486.6 eV) run at 20 mA and 15 kV. The spherical sector analyser was operated in fixed analyser transmission (FAT) mode with a pass energy of 20 eV set across the hemispheres for the high resolution spectra. The instrument calibration procedure was described previously [26]. Sample charging was constant during the analysis so that the energy shifts could be compensated

for by referencing all the spectra to the binding energy of the C1s signal component set at 285.0 eV. The binding energy values reported here are averages of two measurements whose reproducibility was ±0.1 eV. All the spectra were obtained in the digital mode using the Eclipse software running on a IBM 486. The spectra were resolved into their Lorentzian and Gaussian components after subtraction of a linear background. The residual pressure during the data acquisition was of the order of 10^{-9} torr. Samples have been analysed as pellets. Exposure to air was minimised by handling the samples inside a glove bag under argon. XPS measurements were also carried out on the sample used for the EXAFS measurement in order to control the effect of the EXAFS sample preparation procedure.

2.4 X-ray scattering

The SAXS and WAXS patterns were recorded on an instrument consisting of a Philips PW1830 X-ray generator providing CuKα, Ni filtered ($\lambda = 1.5418$ Å) linear beams for both an Anton Paar Kratky compact camera equipped with step scanning motor and scintillation counter and a Philips PW1820 vertical goniometer working in the θ–2θ geometry with step scanning motors and proportional detector. Seven SAXS patterns, in the h-range (0.006–0.6) Å^{-1} ($h = 4\pi \sin(\theta)/\lambda$, 2θ is the scattering angle, λ the incoming wavelength), for an overall counting time of about one day per sample, were recorded with the Kratky camera and summed up; the measurements were carried out under vacuum at 10^{-2} torr; the data were scaled in absolute units per unit volume by a procedure exploiting the moving slit device [27]. The support SAXS data were collected under the same conditions. Accurate WAXS measurements have been performed as well with the PW1820 goniometer: the catalysts and support patterns have been recorded in the 30–90° 2θ range with steps of 0.05° in ten different runs for an overall counting time of more than three days per pattern. Both the SAXS and WAXS different runs did not show any evident structural modifications occurring in the samples in the course of the experiments.

2.5 Transmission electron microscopy

Electron micrographs of the samples A and B were obtained by a Jeol 2000EX TEM microscope equipped with polar piece and top entry stage. Before the introduction in the instrument, the samples, in form of powders, were ultrasonically dispersed in isopropyl alcohol, and a drop of the suspension was deposited on a copper grid covered with a lacey carbon film.

3 Results

3.1 EXAFS

In Figure 1 the EXAFS spectra of the four SMAD samples are reported. The data show good signal to noise ratio despite the low Rh concentrations. Figure 2 reports the k-weighted Fourier Transforms (FT) of the two reference and of the four catalyst samples. The FT of Rh foil is typical of a *fcc* structure. The FT of Rh_2O_3 presents only two peaks: the first is relative to the Rh–O first shell distance, the second is due to Rh–Rh and Rh–O next neighbours' contributions. In the FT of SMAD data it is evident that the first peak corresponds to the position of Rh–O peak in Rh_2O_3, while the second coincides with the first Rh–Rh peak of the metal foil.

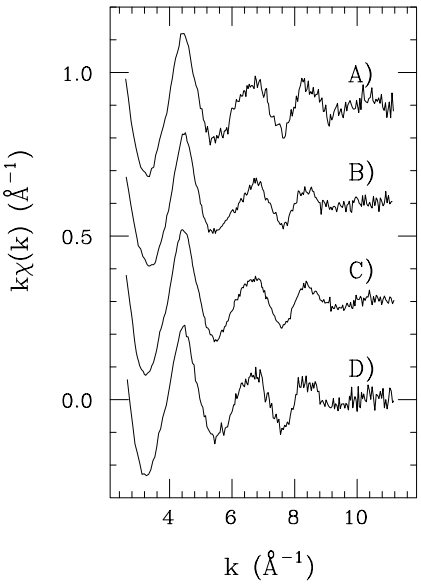

Fig. 1. Experimental EXAFS data for SMAD Rh/pumice catalysts. It must be noted that no appreciable difference occurs between the highest concentration sample (A) and the lower concentration one (D).

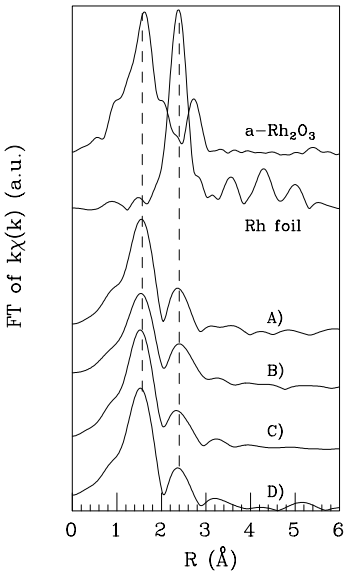

Fig. 2. FT of the EXAFS data of reference samples and of the SMAD catalysts. Dashed lines carefully compare the positions of the two $k\chi(k)$ FT peaks of SMAD catalysts with those of nearest neighbors in reference samples.

The EXAFS signal is given by the oscillations superimposed onto the smooth total atomic absorption coefficient μ_0 and is defined as:

$$\chi(k) = \frac{\mu(k) - \mu_0(k)}{\mu_0(k)} \quad (1)$$

where

$$k = \sqrt{\frac{2m}{\hbar^2}(E - E_0)} \quad (2)$$

is the modulus of the wave-vector of the photoelectron and E_0 the energy value corresponding to the maximum derivative at the absorption edge.

EXAFS is a powerful method to probe the local structure around the absorbing atom either for crystalline or for amorphous materials and standard data analysis methods are well established. Such standard methods are based on the Single Scattering (SS) approximation, which assumes the photo-electron is scattered only once by the surrounding atoms before interfering with the primary wave, and on the Fourier Filtering (FF) technique, which allows separate investigation of the EXAFS contributions of the different coordination shells [28]. A preliminary and qualitative data analysis using the standard approach evidenced, as already shown in Figure 2, two peaks in the FT of Rh/pumice SMAD catalyst: the first one, due to Rh–O, is at 2.04 Å, while the second, ascribed to Rh–Rh, lies at 2.68 Å.

A quantitative and more detailed analysis was carried out using the approach based on the GNXAS package [29,30]. This approach is very suited to studying disordered materials, since it correlates the experimental spectra with the n-body correlation functions in a direct way [29,30]. In these calculations the local atomic arrangement around the absorbing atom is decomposed into model atomic configurations containing only two, three, $\ldots, n$ atoms. For each configuration the atomic phase shifts are calculated using the most opportune exchange and correlation potentials in the muffin-tin approximation. The contributions to the EXAFS signal are expressed in terms of irreducible n-body "$\gamma^{(n)}$" contributions which are calculated considering the effects of all the possible single and multiple scattering (MS) paths between the n-atoms. The theoretical structural signal $\chi(k)$ is given by the sum of the $\gamma^{(n)}$ contributions:

$$\chi(k) = \sum_n \gamma^{(n)}. \quad (3)$$

Multiple scattering effects are negligible in the SMAD catalysts, nevertheless GNXAS uses a rigorous fitting procedure directly on the experimental data [29,30] and carries out a detailed error analysis on fitting parameters to obtain a good confidence on the final results.

GNXAS was first of all applied to the reference samples. Starting from Rh_2O_3 and Rh-foil crystalline model $\gamma^{(n)}$ functions, relative to all the possible scattering and MS paths up to about 6 Å were generated. The use of complex Hedin-Lundqvist potentials allowed a correct inclusion of the effects due to inelastic losses. Figure 3 reports the best fit results obtained on the Rh foil and α-Rh_2O_3 data together with all the $\gamma^{(n)}$ contributions employed. In the lower part the residual of the best fit is reported. The experimental $k\chi(k)$ of rhodium oxide was well reproduced by using only three single scattering contributions ($\gamma^{(2)}$) relative to 6 oxygen atoms at 2.03 Å, 3.2 Rh atoms at 2.98 Å and 3 oxygen atoms at 3.4 Å. To reproduce the $k\chi(k)$ of the Rh foil, due to the focusing effect which enhances the multiple scattering contribution to the fourth *fcc* shell, beyond three $\gamma^{(2)}$, also a $\gamma^{(3)}$ contribution was used. Best fit parameters are reported in Table 1. The N values indicate the coordination numbers, R the interatomic distances and σ^2 the EXAFS Debye-Waller factors. The analysis of the reference samples allowed to determine and fix parameters as S_0^2 (at 0.87), correlated

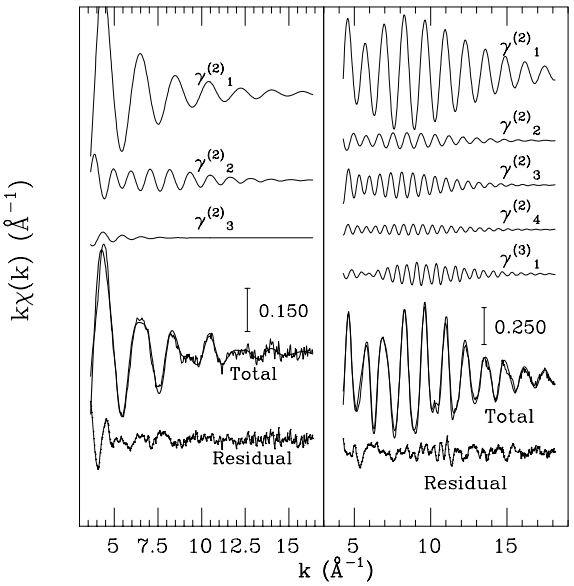

Fig. 3. Best fit results and $\gamma^{(n)}$ contributions for Rh_2O_3 (left panel) and the Rh foil (right panel).

Table 1. EXAFS structural parameters obtained fitting the reference samples experimental data.

	α-Rh_2O_3		Rh-foil
N_{Rh-O}	6.0 (0.3)	N_1	12.0 (0.3)
R_{Rh-O} (Å)	2.04 (0.02)	R_1 (Å)	2.68 (0.02)
σ^2_{Rh-O} (10^{-3} Å^2)	3.0 (0.2)	σ_1^2 (10^{-3} Å^2)	2.8 (0.2)
N_{Rh-Rh}	3.0 (0.2)	N_2	6.0 (0.2)
R_{Rh-Rh} (Å)	3.01 (0.02)	R_2 (Å)	3.75 (0.02)
σ^2_{Rh-Rh} (10^{-3} Å^2)	9.0 (0.3)	σ_2^2 (10^{-3} Å^2)	5.5 (0.3)
N_{Rh-O}	3.0 (0.2)	N_3	24.0 (0.4)
R_{Rh-O} (Å)	3.47 (0.05)	R_3 (Å)	4.67 (0.02)
σ^2_{Rh-O} (10^{-2} Å^2)	2.0 (0.3)	σ_3^2 (10^{-3} Å^2)	7.5 (0.3)
		N_4	12.0 (0.3)
		R_4 (Å)	5.36 (0.03)
		σ_4^2 (10^{-3} Å^2)	5.7 (0.3)
		θ (°)	178 (2.0)

Table 2. Structural parameters obtained by fitting the SMAD catalysts experimental data.

		Samples			
		A	B	C	D
$\gamma_1^{(2)}$	$N_{\mathrm{Rh-O}}$	2.8 (0.3)	2.6 (0.3)	2.9 (0.3)	3.0 (0.3)
	$R_{\mathrm{Rh-O}}$ (Å)	2.04 (0.03)	2.04 (0.02)	2.04 (0.03)	2.04 (0.03)
	$\sigma^2_{\mathrm{Rh-O}}$ (10^{-3} Å^2)	1.6 (0.3)	2.7 (0.3)	2.1 (0.3)	2.2 (0.3)
$\gamma_2^{(2)}$	$N_{\mathrm{Rh-Rh}}$	1.4 (0.3)	1.5 (0.5)	1.0 (0.2)	1.0 (0.2)
	$R_{\mathrm{Rh-Rh}}$ (Å)	2.68 (0.03)	2.68 (0.02)	2.68 (0.03)	2.68 (0.03)
	$\sigma^2_{\mathrm{Rh-Rh}}$ (10^{-3} Å^2)	7.0 (0.3)	8.4 (0.4)	6.4 (0.5)	6.5 (0.5)

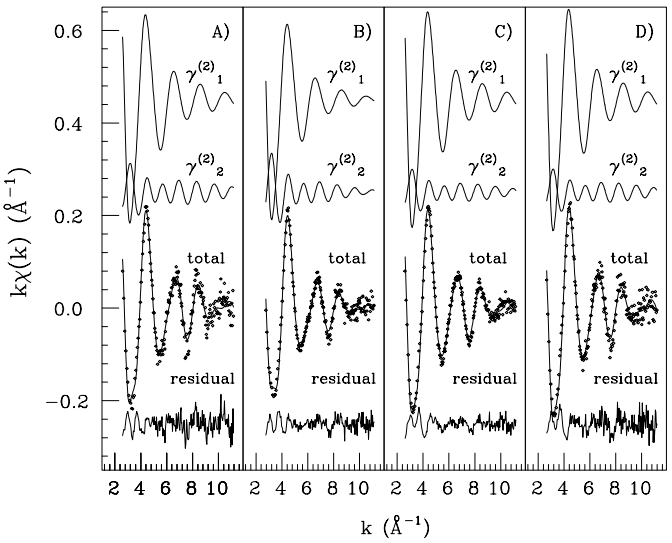

Fig. 4. Experimental $k\chi(k)$ data (dots) and best fits of SMAD Rh/pumice catalysts with the $\gamma^{(n)}$ contributions used and the residual functions.

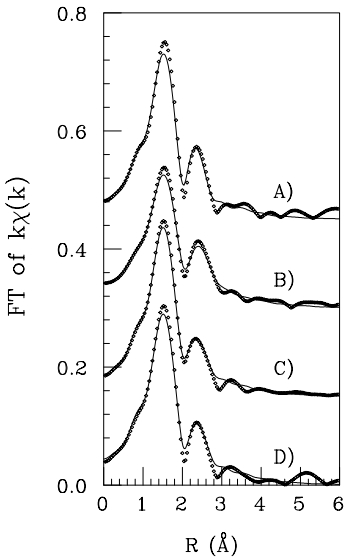

Fig. 5. Comparison of $k\chi(k)$ FT for the experimental data (dots) and best fits (full line).

to the coordination numbers, and the edge energy, E_0 (at 23.315 keV), correlated to the interatomic distances.

SMAD catalysts data were fitted in the k-range 3.5–12 Å^{-1}. Figure 4 shows experimental (dots) and theoretical EXAFS data together with the $\gamma^{(n)}$ contributions used in the best fit. The residuals of the best fits are also reported. Best fit parameters are summarised in Table 2. Figure 5 shows the FT of the experimental data (dots) and of the best fits (full lines). The statistical errors on parameters were evaluated by the dimension of the ellipse which encloses, in the parameter space, χ^2 values with a confidence of 95% [29]. All the catalysts' EXAFS data were well fitted using only two $\gamma^{(2)}$ contributions representing Rh–O and Rh–Rh correlations whose R-values are respectively equal to those found for Rh_2O_3 and Rh foil (Tab. 1). The Rh–Rh contribution at 2.98 Å, which is typical of the Rh_2O_3, was rejected by the fitting routine.

The coordination numbers, $N_{\mathrm{Rh-O}} \sim 3$ and $N_{\mathrm{Rh-Rh}} \sim 1.5$, are clearly different from those found in the reference samples. Since the Rh atoms are present in two different states (oxide and metal) a simple application of the EXAFS formula cannot give the true Rh–O and Rh–Rh coordination numbers, that could be obtained by weighting the calculated ones by the fractions of metallic and oxide phases.

3.2 XPS

In Figure 6 a typical Rh $3d$ spectrum of the B sample is shown. The spectrum, formed by the two spin orbit components $3d_{5/2}$ and $3d_{3/2}$, is characterised by two doublets corresponding to two different chemical states of rhodium. The position of the $3d_{5/2}$ lines, at 307.4 eV and 309.3 eV are typical of a metallic state and of a highly oxidised state, respectively [12]. From the area measurements of the peaks the ratio of the oxidised form to the metal is approximately 2 to 1.

3.3 X-ray scattering

The log-log plots of the SAXS patterns of the catalysts and of the support, scaled in electronic units, are reported in Figure 7. It can be observed that the pumice small-angle pattern shows in the central part a h^{-3} slope and from $h > 0.2$ a slightly increasing intensity that is probably

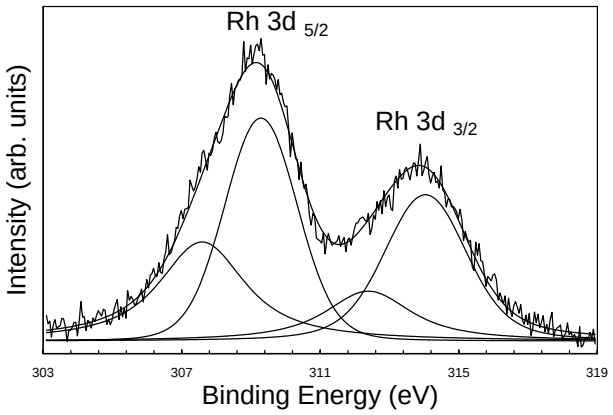

Fig. 6. Rh 3d photoelectron spectra of the B sample. The fitted curve (smooth solid line) is the sum of the $3d_{5/2}$ and $3d_{3/2}$ Rh lines; the metal (dashed) and oxide (dotted) components are shown.

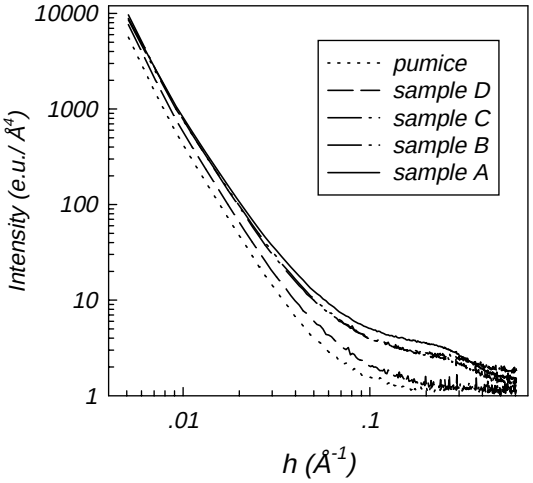

Fig. 7. SAXS curves of the carrier and of the four Rh/pumice SMAD catalysts.

due to the tail of the wide-angle intense diffraction halo typical of amorphous alumino silicates [1].

The most evident feature of the three catalysts with higher Rh content is the shoulder that begins at $h \approx 0.1$ and extends up to the highest measured h values; also the least concentrated sample exhibits in this h range a small angle scattering clearly different from the support one. On the other hand, the central part of the catalysts SAXS curves resembles the support one. Therefore, it is conceivable that also in the catalysts the carrier scattering is mainly given by a Porod term plus a constant background. Recently, the support scattering has been separated by exploiting anomalous SAXS [31,32]; this technique allowed, for carbon-supported metal catalysts, the experimental separation of the carrier scattering and, as a consequence, the determination of the size distribution of the metal particles.

In this study an approach similar to the latter quoted one [33] led, on the assumption of non-interacting spherical particles, to the determination of their size distribution. A library of calculated patterns $I(r_i, h)$ has been created, corresponding to spherical particles of radii r_i ranging from 3 to 31 Å with a step $\Delta r = 0.5$ Å and taking into account the smearing effect due to the finite height of the collimation and detector slit [34]. The smeared calculated intensity per unit volume is given by:

$$I(h) = \alpha h^{-3} + \beta + w_{\mathrm{Rh}} \sum_{r_i} \gamma_i I(r_i, h) \qquad (4)$$

where the first two terms account for the support scattering and the last one is the weighted sum on the library of calculated patterns. The parameter w_{Rh} is the overall weight of the Rh phase with respect to the support scattered intensity and takes into account also the excess scattering density of the Rh particles. The γ_i weights, corresponding to a lognormal size distribution [33], are given by:

$$\gamma_i \propto \frac{1}{\sqrt{2\pi}} \frac{1}{\sigma} \frac{\Delta r}{r_i} \exp\left[-\frac{\ln^2(r_i/r_0)}{2\sigma^2}\right] \qquad (5)$$

where r_0 is the median and σ the shape parameter; the γ_i values are dimensionless numbers, giving the frequency of the r_i cluster. The proportionality symbol in equation (5) allows for the γ_i normalization that is achieved by dividing by their sum.

The α, β, w_{Rh}, r_0 and σ parameters have been determined by least squares fitting of equation (4) to the SAXS data in the (0.04, 0.6) h-interval. A representative fitting result is reported in Figure 8 for the A sample and the overall results for the A, B and C samples are summarised in Table 3; the SAXS analysis performed on the D sample did not give reliable results, likely owing to the very small metal amount. In Figure 9 the γ values corresponding to the other three samples are drawn; the normalization factor is almost equal to one (0.999 7 in the worse case, sample A). From inspection of Table 3 and Figure 9, it is possible to see that, according to the SAXS

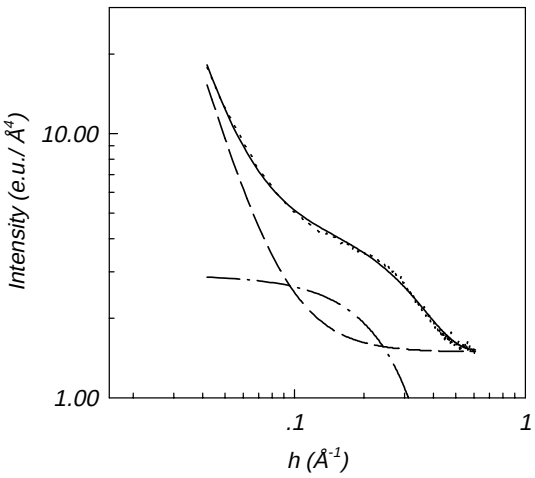

Fig. 8. Fitting of equation (4) to the SAXS data of sample A in the (0.04, 0.6) h interval. The fitted total curve (solid line), the carrier intensity (dashed line), and the Rh particles scattering (dash-dotted line) are shown.

Table 3. Parameters relative to the Rh/pumice A, B, C samples, as determined by the fitting of equation (4) to the respective SAXS data.

	r_0 (Å)	σ	w_{Rh} ($\times 10^{-6}$) (eu/Å^9)	α ($\times 10^{-3}$) (eu/Å)	β (eu/Å^4)
A	6.66(1)	0.036(4)	1.05(3)	1.01(1)	1.47(3)
B	6.6(2)	0.08(4)	0.55(1)	0.88(2)	1.39(2)
C	6.06(5)	0.14(2)	0.55(3)	0.85(1)	1.8(1)

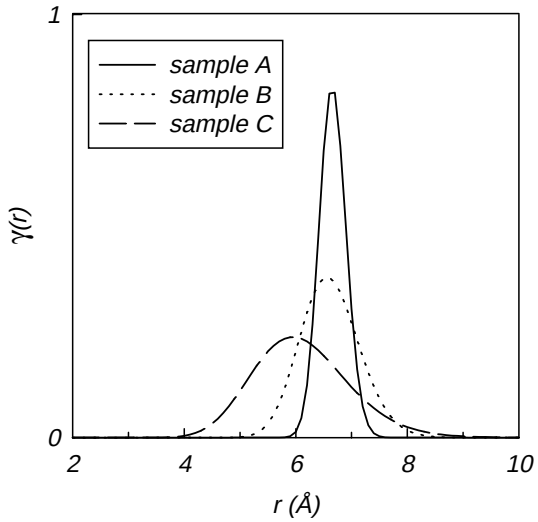

Fig. 9. γ weights relative to the r_0 and σ parameters of equation (5), as determined by the fitting of equation (4) to the SAXS data of the A, B and C samples, respectively. The γ values are drawn, for a clearer view, as continuous $\gamma(r)$ functions.

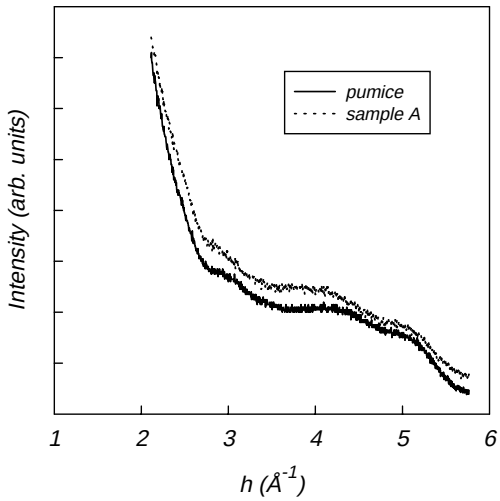

Fig. 10. WAXS patterns of the carrier (bottom) and of the A sample (top line).

analysis, there is a slight increase of the average particle size with the metal loading, whereas the width of the size distribution becomes narrower. The variation of the overall metal weight w_{Rh} is in agreement with the chemical analysis.

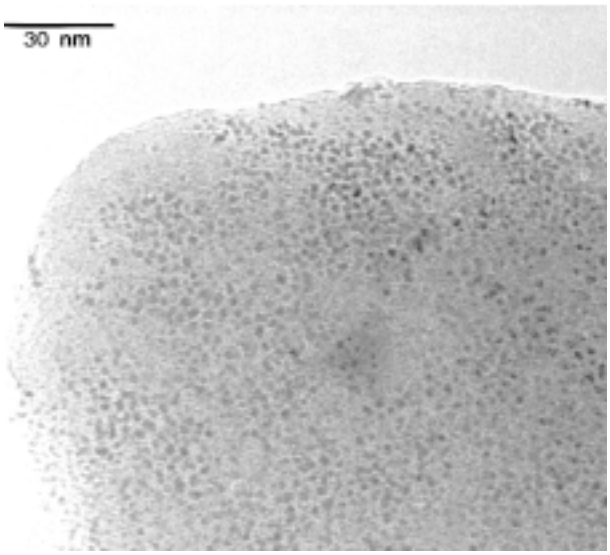

Fig. 11. TEM micrograph relative to sample B.

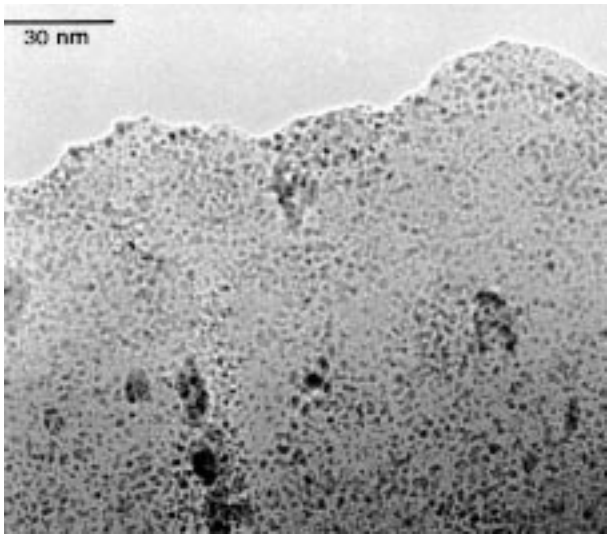

Fig. 12. TEM micrograph relative to sample A.

In Figure 10 the WAXS pattern of the A sample is reported. It is clear that no crystalline peak can be observed and therefore that crystalline particles, if any, either oxides or metallic *fcc*, are on the average very small (less than 20 Å) and probably disordered.

3.4 TEM

Figure 11 reports a TEM image of sample B. The pumice surface appears densely populated by small supported particles, quite homogeneously distributed onto the carrier. In the case of sample A, which contains higher amounts of Rh, supported particles appear slightly larger in size and more densely distributed on the support (Fig. 12). Furthermore, a few large structures are present, produced by agglomeration of several particles.

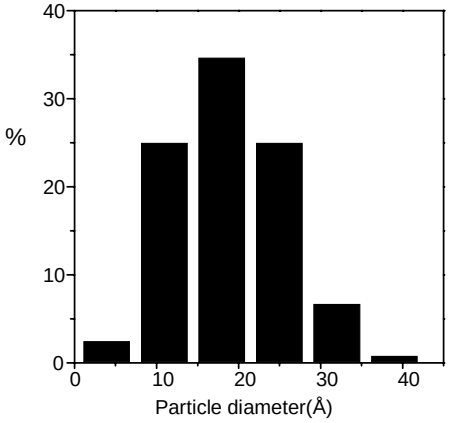

Fig. 13. Histogram relative to the size distribution of sample B, as determined by the analysis of the relevant TEM micrograph.

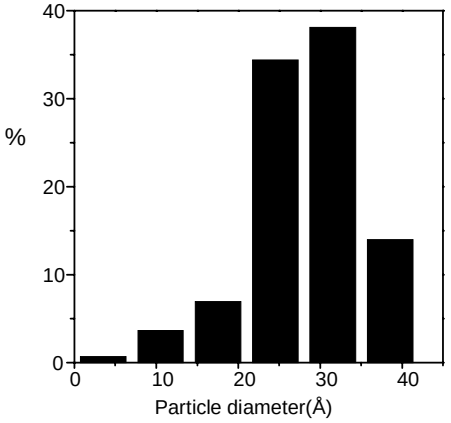

Fig. 14. Histogram relative to the size distribution of sample A, as determined by the analysis of the relevant TEM micrograph.

Histograms of the metal particle size distribution were obtained by counting onto the micrographs at least 300 particles, and the mean particle diameter (d_{m}) was calculated by using the formula $d_{\mathrm{m}} = \sum d_i n_i / \sum n_i$, where n_i was the number of particles of diameter d_i. The counting was carried out on electron micrographs taken at 150 000 magnification, where Rh particles well contrasted with respect to the support were clearly detected. In this condition the uncertainty in the measurement of the size of the supported particles was ± 3 Å. Histograms of the supported particles size distribution (SPSD) for sample B and A, respectively, are reported in Figures 13 and 14. For sample B, containing a lower loading of Rh, the SPSD is centered at lower values, and a mean diameter $d_{\mathrm{m}} = 17 \pm 3$ Å was calculated (Fig. 13). In the case of sample A, an overwhelming fraction of Rh-bearing particles with size in the 20–35 Å range was observed, resulting in a mean diameter $d_{\mathrm{m}} = 27 \pm 3$ Å (Fig. 14). Noticeably, in both cases very small supported particles (less than 15 Å in size) are present, their relative amount being quite important (*ca.* 25%) for sample B.

Table 4. Hydrosilylation of benzonitrile with $HSiMe_3$ catalysed by Rh systems[a].

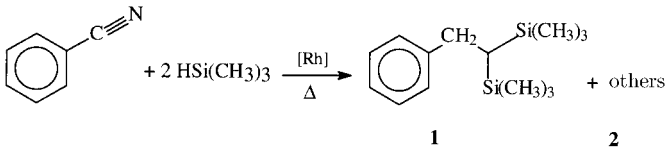

1 **2**

Catalyst (Rh wt%)	Conv. (%)	Product distribution (%)	
		1	**2**
Rh/pumice (0.8%)	100	100	–
Rh/γ-Al_2O_3 (0.8%)	80	100	–
Rh/γ-Al_2O_3 comm. (3%)	30	5	95[b]

[a]Reaction conditions: nitrile (9.8 mmol); hydrosilane (49 mmol); Rh (0.1 mg atom); $T = 100$ °C; *time* = 5 h.
[b]Mixture of oligomers.

3.5 Catalytic tests

The catalytic tests on the Rh/pumice systems are being carried out. Preliminary experiments indicate that the above systems are able to promote the catalytic hydrosilylation of aromatic nitriles to N, N-disilylamines in unusual high yield. The results obtained in the hydrosilylation of benzonitrile with trimethylsilane using SMAD-prepared Rh/pumice and Rh/γ-Al_2O_3 catalysts and a commercial Rh/γ-Al_2O_3 sample are reported in Table 4.

4 Discussion

4.1 Chemical environment of Rh

The conclusion of the EXAFS analysis is that in all the SMAD samples the Rh atoms are part in a highly oxidised state, probably Rh^{+3}, according to EXAFS and part in a metallic Rh^0 state. The XPS analysis performed on sample B confirms that rhodium can be found in the Rh^{+3} state (but also Rh^{+4} cannot be excluded [12]) or in the metallic one. The ratio of 2:1 found for the relative abundance of the two states cannot be used to determine the real coordination numbers in the EXAFS analysis because XPS is more sensitive to the surface composition, whereas EXAFS is a bulk technique. However, it is worth noticing that the XPS analysis performed on the specifically prepared sample and on the EXAFS one gave similar results, confirming that the Rh oxidation did not take place during the manipulations for the EXAFS experiments.

The Rh–O and Rh–Rh bond lengths found by EXAFS in the present study are not very different from the values found by Martens *et al.* [35]; the coordination numbers

are also similar. In the above quoted paper the oxidation process of Rh/Alumina samples that were initially reduced in hydrogen flow at 623 K was followed by *in situ* EXAFS. The reduction process is rather drastic, so that only a weak interaction of Rh with the support oxygens and a preponderant metal phase was seen. Afterword, the samples were oxidised by oxygen flow and a Rh–O distance similar to ours was detected. On the contrary, the reduction process in the Rh/pumice SMAD samples is indeed very mild, consisting merely of the solvent molecules stripping by vacuum pumping. The bare Rh atoms that are produced by this process are very reactive (as it is also demonstrated by the Rh/mesitylene solid residue on the reactor walls, that, in presence of air, develops a highly esothermic reaction) and are responsible for the formation of the rhodium oxide phase by a strong interaction with the support. The metal particles likely grow on this interlayer. The mechanism has been already acknowledged by Tan *et al.* [21] who used Mn as a sacrificial species to build up the interlayer between cobalt (the real catalyst) and the silica support.

4.2 Structural aspects

The absence of peaks in the WAXS patterns point to the presence of a highly dispersed Rh phase, with particle size less than 20 Å, in the investigated Rh/pumice catalysts. On a more quantitative ground, the analysis of the SAXS patterns gives values of about 6–7 Å for the radii of the supported metal-bearing particles corresponding to the three catalysts with higher Rh content. The comparison between the TEM results (Figs. 13 and 14) and the SAXS ones (Tab. 3 and Fig. 9) evidences that, whereas the agreement between the two techniques is good enough for sample B, different size values are given for sample A. A previous structural study on Pd/pumice catalysts, involving as well the SAXS-TEM comparison [36], gave satisfactory results for a low-metal content sample, whereas the discrepancy was severe for a sample showing aggregation of the metal particles. In fact, as demonstrated also by other studies [37], TEM suffers from a lack of resolution power in dealing with aggregated particles. In the above quoted paper, for instance, disagreement with EXAFS was recognised when the number of Rh–Rh neighbours in polymer-protected Rh clusters was related to the average particle size. The Rh/pumice SMAD samples probably give further trouble with TEM, because the electron beam can produce, as for other SMAD systems [38], merging of neighbouring particles. Being aware of this possibility, the electron beam intensity was kept as low as possible, but it cannot be excluded that some sintering (and even some reduction of the oxide phase) has been produced, especially in the higher content Rh sample.

In agreement with the EXAFS results that do not evidence remarkable structural differences between the investigated samples, the SAXS indicates that there is only a slight increase of the average particle size with the metal loading. Therefore, taking into account that TEM also reports for the presence of the small particles detected by SAXS, it could be conceived that in the analysed h range SAXS puts into evidence the primary Rh particles, that are very small (6–7 Å radius) and partly agglomerated to constitute larger ones, best seen by TEM. The most evident SAXS signal from the Rh phase lies at relatively high values of momentum transfer (Fig. 7), corresponding therefore to higher resolution. Probably, at smaller h-values, the SAXS pattern should show the scattering of the aggregates as a whole particle, but this range couldn't be reliably analysed, due to the overwhelming support scattering. The presence of small Rh particles despite the Rh–Rh distance not differing from that of the Rh bulk, is in agreement with previous works [37,39].

It is not possible to exclude that the metallic and oxidised Rh particles are distinct and/or characterised by different size and shape; however, according to the above reported considerations on the chemical environment of the Rh atoms, it looks feasible that the Rh-bearing particles are oxidised in contact with the carrier and afterword continue as metallic. Electron diffraction analyses, carried out in order to establish the metallic or oxide nature of the observed particles, were too poorly defined to get reliable information about this point.

It is hard to get from the EXAFS analysis the real coordination numbers, that could give an indication about the size of the metallic and oxidised domains, because the calculated ones, reported in Table 2, should be corrected by the respective relative amounts of the two phases. Martens *et al.* [35] gave a range of values for the corrected coordination numbers by assuming that the oxidised Rh phase have four to six oxygens at about 2.05 Å. If, by a somewhat reversed approach, we consider for the first shell real coordination numbers of the metallic domains a range of values from 12 (corresponding to huge particles) to 4.5 (Rh clusters of 3 Å radius, according to the recently proposed [40] *bond model* for spherical clusters), we get metallic phase fractions ranging, for the B sample, from 0.13 to 0.33. The upper limit corresponds to the value afforded by the XPS analysis for the B sample. Taking into account that XPS is a surface technique, and that the allowed coordination number interval is fairly wide, it looks reasonable to argue that the metallic phase lies mostly at the exterior of the supported rhodium particles.

4.3 Catalytic activity

From inspection of the results reported in Table 4, it can be seen that the Rh vapour derived catalysts are largely more active than the commercial sample giving the hydrosilylation product with complete selectivity. The commercial sample shows a very poor activity and selectivity, affording prevalently a complex mixture of oligomers as main reaction products. It is worth noting that the Rh/pumice catalyst is slightly more active than the corresponding Rh/γ-Al_2O_3 sample indicating that the small area of the support is not detrimental for the reactivity; on the contrary it could facilitate a more favourable exposure of the catalytic sites.

5 Conclusions

In this study a thorough structural characterization of Rh/pumice SMAD catalysts have been carried out. The exploited spectroscopic techniques agree that a good deal of the Rh atoms have been oxidised as a consequence of the supporting route. The hypothesis that the oxidation is due to the interaction with the available hydroxyls of the support, already put forth for other SMAD systems [21], is corroborated by the comparison between the XPS and the EXAFS results. The formation of rhodium aluminates and/or silicates at the Rh/pumice interface could be conceivable. All the structural evidences point to very small and, probably, disordered Rh-bearing particles. SAXS and TEM give not very different values of particle sizes for the sample B, whereas the discrepancy is more pronounced, and critically analysed, for sample A.

The high selectivity of the Rh/pumice systems mirrors that of Pd/pumice catalysts [3,5] and the specific activity, that looks likely to be comparable with that of a Rh/γ-Al_2O_3 SMAD sample and definitely higher than a commercial one, constitute a further confirmation that the low surface area is not detrimental, in the presence of efficient dispersion techniques, for the preparation of good catalysts.

This study has been carried out with the financial support of CNR (Progetto Finalizzato MSTA II), of MURST (60% and 40% funds) and of Pumex SpA. The assistance and precious advice of the scientific staff of the beamline GILDA at ESRF is also gratefully acknowledged.

References

1. G. Deganello, L.F. Liotta, A. Longo, A. Martorana, Y. Yanev, N. Zotov, J. Non-Cryst. Solids **232**, 547 (1998).
2. M. Boutonnet, J. Kizling, V. Mintsa-Eya, A. Choplin, R. Touroude, G. Maire, P. Stenius, J. Catal. **103**, 95 (1987).
3. G. Deganello, D. Duca, A. Martorana, A. Benedetti, G. Fagherazzi, J. Catal. **150**, 127 (1994).
4. A.M. Venezia, L.F. Liotta, G. Deganello, Z. Schay, L. Guczi, J. Catal. (submitted, 1999).
5. D. Duca, L.F. Liotta, G. Deganello, J. Catal. **154**, 69 (1995).
6. L.F. Liotta, A.M. Venezia, A. Martorana, G. Deganello, J. Catal. **171**, 177 (1997).
7. A.M. Venezia, A. Rossi, L.F. Liotta, A. Martorana, G. Deganello, Appl. Catal. A **147**, 81 (1996).
8. S. Siegel, in *Comprehensive Organic Synthesis*, edited by B.M. Trost, I. Fleming (Pergamon, Oxford, 1991), Vol. 8, p. 417.
9. M. Beller, B. Cornils, C.D. Frohning, C.W. Kohlpainter, J. Mol. Catal. A: Chem. **104**, 17 (1995).
10. I. Ojima, in *The Chemistry of Organic Silicon Compounds*, edited by S. Patai, Z. Rappoport (Wiley, New York, 1989), p. 1479.
11. P. Johnston, R.W. Joyner, P.D.A. Pudney, E.S. Shpiro, B.P Williams, Farad. Discuss. Chem. Soc. **89**, 91 (1990).
12. Z. Weng-Sieh, R. Gronsky, A.T. Bell, J. Catal. **170**, 62 (1997).
13. K.K. Bando, K. Asakura, H. Arakawa, K. Isobe, Y. Iwasawa, J. Phys. Chem. **100**, 13636 (1996).
14. K. J. Klabunde, Y.X. Li, B.J. Tan, Chem. Mater. **3**, 30 (1991).
15. C. Polizzi, A.M. Caporusso, G. Vitulli, P. Salvadori, J. Organomet. Chem. C **4**, 451 (1993).
16. S. Bertozzi, N. Campigli, G. Vitulli, R. Lazzaroni, P. Salvadori, J. Organomet. Chem. **41**, 487 (1995).
17. G. Vitulli, R. Falorni, P. Salvadori, A. Parmaliana, F. Frusteri, N. Giordano, Catal. Lett. **17**, 151 (1993).
18. G. Vitulli, E. Pitzalis, P. Salvadori, G. Capannelli, O. Monticelli, A. Servida, A. Julbe, Catal. Today **25**, 249 (1995).
19. G. Vitulli, E. Pitzalis, R. Lazzaroni, P. Pertici, P. Salvadori, O. Salvetti, S. Coluccia, G. Martra, Mat. Science For. **195**, 93 (1995).
20. G. Vitulli, A. Verrazzani, E. Pitzalis, P. Salvadori, G. Capannelli, G. Martra, Catal. Lett. **44**, 205 (1997).
21. B.J. Tan, K.J. Klabunde, T. Tanaka, H. Kanai, S. Yoshida, J. Am. Chem. Soc. **110**, 5951 (1988).
22. J.L.G. Fierro, *Spectroscopic Characterization of Heterogeneous Catalysts* (Elsevier, Amsterdam, 1990), part A.
23. O.W. Steward, O.R. Pierce, J. Am. Chem. Soc. **83**, 1916 (1961).
24. S. Pascarelli, F. D'Acapito, G. Antonioli, A. Balerna, F. Boscherini, R. Cimino, G. Dalba, P. Fornasini, G. Licheri, C. Meneghini, F. Rocca, S. Mobilio, ESRF Newslett. **23**, 17 (1995).
25. S. Pascarelli, F. Boscherini, F. D'Acapito, J. Hrdy, C. Meneghini, S. Mobilio, J. Synch. Rad. **3**, 147 (1996).
26. A.M. Venezia, A. Rossi, D. Duca, A. Martorana, G. Deganello, Appl. Catal. A **125**, 113 (1995).
27. S. Polizzi, N. Stribeck, H.G. Zachmann, R. Bordeianu, Colloid Polym. Sci. **267**, 281 (1989).
28. P.A. Lee, P.H. Citrin, P. Eisenberger, B.M. Kinkaid, Rev. Mod. Phys. **53**, 769 (1981).
29. A. Filipponi, A. Di Cicco, C.R. Natoli, Phys. Rev. B **52**, 15122 (1995).
30. A. Filipponi, A. Di Cicco, Phys. Rev. B **52**, 15135 (1995).
31. A. Benedetti, S. Polizzi, P. Riello, F. Pinna, G. Goerigk, J. Catal. **171**, 345 (1997).
32. H.-G. Haubold, X.K. Wang, Nucl. Instr. Meth. Phys. Res. B **97**, 50 (1995).
33. H.-G. Haubold, X.H. Wang, G. Goerigk, W. Schilling, J. Appl. Cryst. **30**, 653 (1997).
34. O. Glatter, O. Kratky, *Small Angle X-ray Scattering* (Academic Press, London, 1982), Chap. 4.
35. J.H.A. Martens, R. Prins, D.C. Konigsberger, J. Phys. Chem. **93**, 3179 (1989).
36. G. Fagherazzi, A. Benedetti, G. Deganello, D. Duca, A. Martorana, G. Spoto, J. Catal. **150**, 117 (1994).
37. M. Harada, K. Asakura, Y. Ueki, N. Toshima, J. Phys. Chem. **97**, 10742 (1993).
38. G. Martra, S. Coluccia, O. Monticelli, G. Vitulli, Catal. Lett. **29**, 105 (1994).
39. J.B.A.D. van Zon, D.C. Koningsberger, H.F.J. van't Blik, D.E. Sayers, J. Chem. Phys. **82**, 5742 (1985).
40. M. Borowski, J. Phys. IV France **7**, C2–259 (1997).